Sound-driven single-electron transfer in a tunable beam-splitter setup

Shintaro Takada[1,2,†], Hermann Edlbauer[1,†], Hugo V. Lepage[3], Junliang Wang[1], Pierre-André Mortemousque[1], Giorgos Georgiou[1,4], Crispin H. W. Barnes[3], Chris J. B. Ford[3], Mingyun Yuan[5], Paulo V. Santos[5], Xavier Waintal[6], Arne Ludwig[7], Andreas D. Wieck[7], Matias Urdampilleta[1], Tristan Meunier[1] & Christopher Bäuerle[1,⋆]

[1] Univ. Grenoble Alpes, CNRS, Institut Néel, 38000 Grenoble, France

[2] National Institute of Advanced Industrial Science and Technology (AIST), National Metrology Institute of Japan (NMIJ) 1-1-1 Umezono, Tsukuba, Ibaraki 305-8563, Japan

[3] Cavendish Laboratory, Department of Physics, University of Cambridge Cambridge CB3 0HE, United Kingdom

[4] Univ. Savoie Mont-Blanc, CNRS, IMEP-LAHC, 73370 Le Bourget du Lac, France

[5] Paul-Drude-Institut für Festkörperelektronik, Hausvogteiplatz 5-7, 10117 Berlin Germany

[6] Univ. Grenoble Alpes, CEA, INAC-Pheliqs, 38000 Grenoble, France

[7] Lehrstuhl für Angewandte Festkörperphysik, Ruhr-Universität Bochum Universitätsstraße 150, 44780 Bochum, Germany

[†] these authors contributed equally to this work

[⋆] corresponding author: christopher.bauerle@neel.cnrs.fr

Surface acoustic waves (SAWs) strongly modulate the shallow electric potential in piezoelectric materials. In semiconductor heterostructures such as GaAs/AlGaAs, SAWs can thus be employed to transfer individual electrons between distant quantum dots[1–3]. This transfer mechanism makes SAW technologies a promising candidate to convey quantum information through a circuit of quantum logic gates[4,5]. Here we present two essential building blocks of such a SAW-driven quantum circuit. First, we implement a triggered single-electron source enabling synchronisation of SAW-driven transport along parallel paths. Then, we couple a pair of transport channels via a tunnel barrier to partition a flying electron arbitrarily into the two paths. All of the presented single-shot experiments are performed with a transfer efficiency exceeding 99 %. Our results open up the way to perform quantum logic operations on the fly and show that a SAW-driven integrated circuit is feasible with single electrons on a large scale.

DiVincenzo's criteria for realising a quantum computer address the transmission of quantum information between stationary nodes[6]. Several approaches have demonstrated successful transmission of quantum states in solid-state devices such as in quantum dot (QD) arrays[7–9] or microwave-coupled superconducting qubits[10,11]. In semiconductor heterostructures, surface acoustic waves (SAWs) offer a particularly interesting platform to transmit quantum information. Thanks to the shallow electric potential modulation on a piezoelectric substrate, a SAW forms a train of moving QDs along a depleted transport channel. This SAW train allows to drag single charge carriers from one side of such a quantum rail to the other. Employing stationary QDs as electron source and receiver, a single electron has been sent back and forth several micrometer long tracks with a transfer efficiency of about 92 %[1,2]. Recently, SAW-driven transfer of individual spin polarized electrons has been reported[3]. These advances support the idea of a SAW-driven quantum circuit enabling the implementation of electron quantum optics experiments[5,12–14] and quantum computation schemes at the single-particle level[15,16]. The central building block of such a quantum circuit is a tunable beam splitter permitting the coupling and partitioning of single flying electrons. The experimental implementation of such a device, however, is still missing.

In this work we investigate the feasibility of such a beam splitter setup for SAW-driven single-electron transport. In order to realise quantum logic gates, where a pair of electrons are made to interact in flight, it is necessary to synchronise transport. To achieve precise control of the sending process, we realise a SAW-driven single-electron source that is triggered by a voltage pulse on the timescale of picoseconds. To realise beam splitter operation, we then couple a pair of quantum rails by a tunnel barrier and partition an electron into the two output channels. Modeling the experimental results of this directional-coupler operation with quantum mechanical simulations, we deliver insight into the quantum state of the flying electron and discuss the remaining challenges to implement quantum logic gates for SAW-transported flying charge qubits[5,17,18].

The SAW-driven single-electron beam splitter is realised via surface electrodes forming a depleted potential landscape in the two-dimensional electron gas (2DEG) of a GaAs/AlGaAs heterostructure. An interdigital transducer (IDT) is used to send a finite SAW train towards our single-electron circuit as shown schematically in Fig. 1a. The SAW allows the transport of a single electron from one gate-defined QD (source) to another stationary QD (receiver) through a circuit of quantum rails. Figure 1b shows a

scanning-electron-microscopy (SEM) image of a source QD with a schematic description of the electrical connections. To detect the presence of an electron, a quantum point contact (QPC) is placed next to the QD. By biasing this QPC at a sensitive working point, an electron leaving or entering the QD can be detected by a jump in the current, I_{QPC}[19]. A SEM image of the whole single-electron circuit is shown in Fig. 1c. The device consists of two quantum rails having a total length of 22 μm. The transport channels are coupled along a region of 2 μm by a tunnel barrier defined by a 20-nm-wide surface gate.

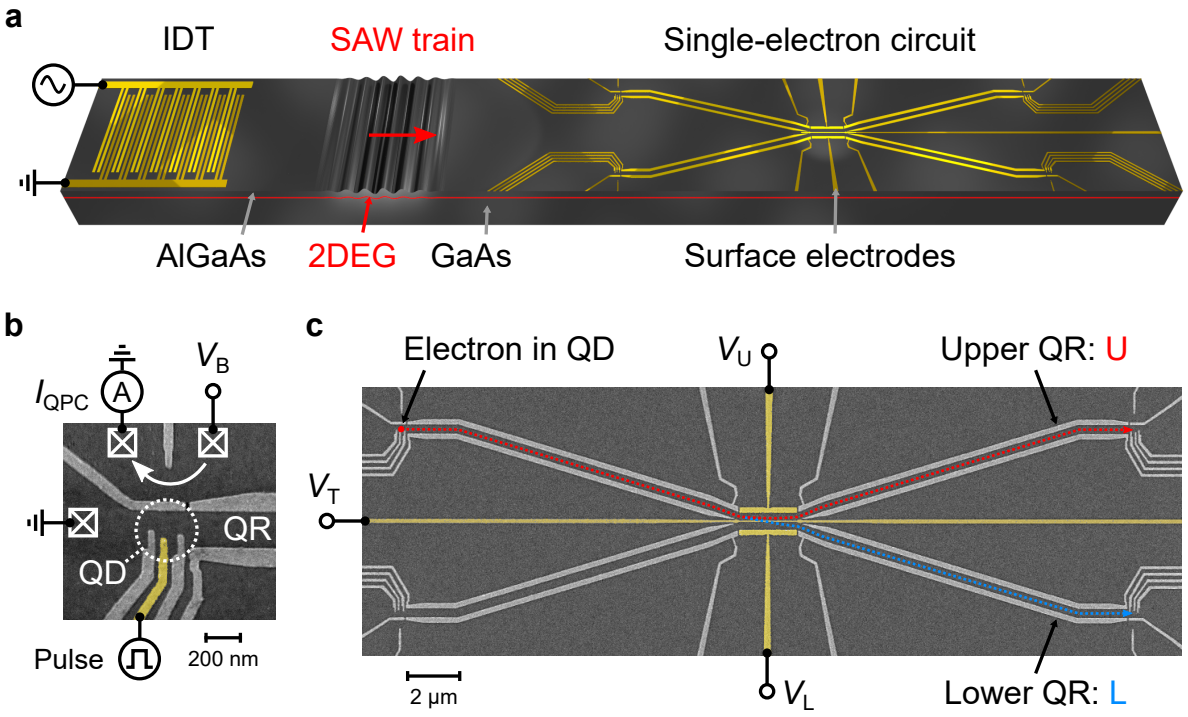

Fig. 1: Experimental setup. **(a)** Schematic showing an interdigital transducer (IDT) launching a SAW train towards the single-electron circuit. **(b)** SEM image of the upper source quantum dot (QD), which is coupled to the quantum rail (QR) with the schematically indicated electrical connections. **(c)** SEM image showing the tunnel-coupled quantum rails with schematically indicated transport paths, U and L.

To quantify the efficiency of SAW-driven single-electron transfer, we decouple the quantum rails by setting a high tunnel-barrier potential using a gate voltage of $V_{\mathrm{T}} = -1.2$ V. We deduce the transfer efficiency based on the data from 70,000 SAW-driven single-electron transfer experiments – see Supplementary Section A. Thanks to the low error rates of loading (0.07 %) and catching (0.18 %), we achieve a transfer efficiency along our 22-μm-long quantum rail of 99.75 %.

The extremely high transfer efficiency makes SAW-driven single-electron transport a promising candidate to couple a pair of electrons in such a beam-splitter setup. In the long run, this coupling could enable entanglement of single flying electron qubits[5]. To tread this path, electrons must be sent simultaneously from different sources in a specific position of the SAW train. We accomplish this requirement using a 90 ps voltage pulse, which we employ to trigger electron transport. Figure 2a shows a SEM image of a source QD with the pulsing gate highlighted in yellow. After loading an electron from the reservoir, we bring the particle into an isolated configuration where it cannot be picked up by the SAW. To load the electron into a specific minimum of the SAW train, we apply a voltage pulse at the right moment to the plunger gate of the QD as schematically shown in Fig. 2b. This pulse allows the electron to escape the stationary source QD into a specific moving QD formed by the SAW along the quantum rail.

To demonstrate the feasibility of this trigger, we use an ultrashort voltage pulse of 90 ps[20] corresponding to a quarter SAW period. Sweeping the delay of this pulse, τ, over the arrival window of the SAW at the source QD, we observe distinct fringes of transfer probability as shown in Fig. 2c and more detailed in Fig. 2d. The data shows that the fringes are exactly spaced by the SAW period. This periodicity indicates that there is a particular phase along the SAW train where a picosecond pulse can efficiently transfer an electron from the stationary source QD into a specific SAW minimum. As the voltage pulse overlaps in time with this phase, transfer is activated and the efficiency rapidly goes up to (99.0 ± 0.4) %. By reduction of the pulse attenuation and improvement of the QD structure, we anticipate further enhancements in the trigger efficiency. The present pulsing approach allows us to synchronise the transport of single electrons along parallel quantum rails and opens the way to couple single flying electrons.

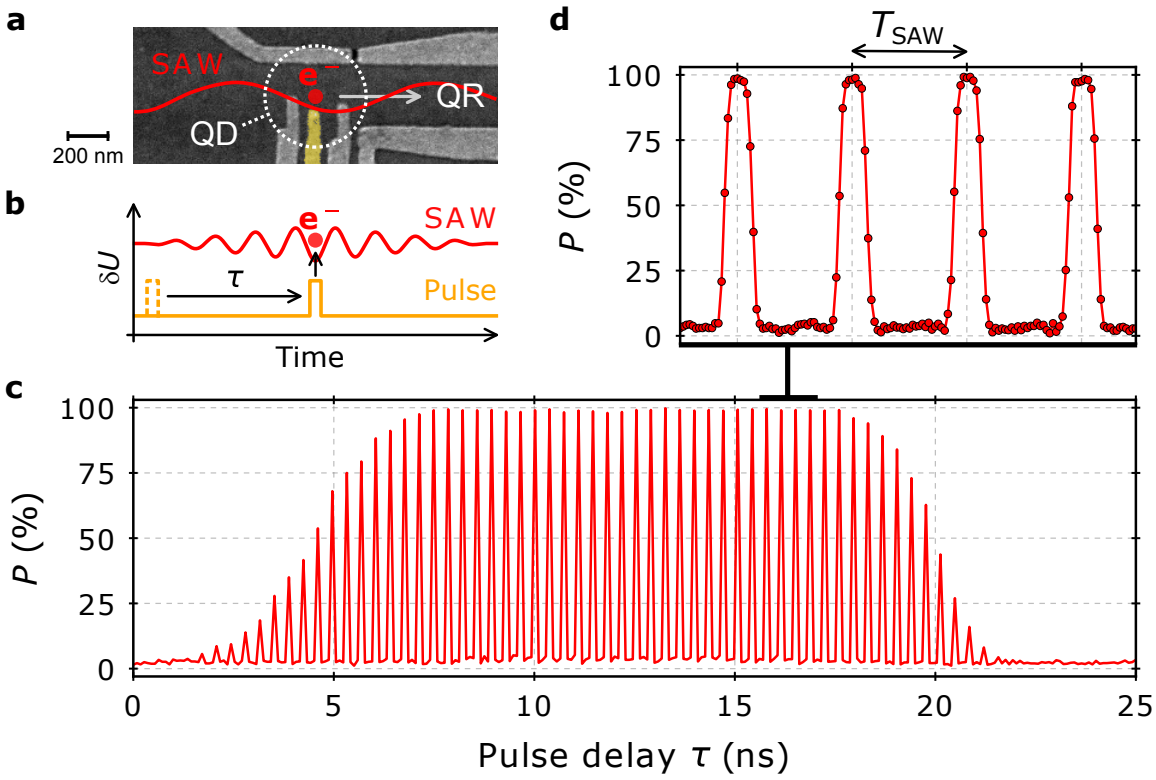

Fig. 2: Pulse-triggered single-electron transfer. **(a)** SEM image of the source quantum dot (QD) showing the pulsing gate highlighted in yellow. A fast voltage pulse on this gate allows one to trigger SAW-driven single-electron transport along the quantum rail (QR). **(b)** Measurement scheme showing the modulation, δU, of the electric potential at the stationary source QD: the delay of a fast voltage pulse, τ, is swept along the arrival window of the SAW. **(c)** Measurement of the probability, P, to transfer a single electron with the SAW from the source to the receiver QD for different values of τ. **(d)** Zoom in on a time frame of four SAW periods, T_{SAW}.

Having established highly efficient single-electron transport, we couple the two channels to partition an electron in flight between the two quantum rails. The aim of this tunnel coupling is to prepare a superposition state of a flying qubit. We find that we can finely control the partitioning of the electron, by detuning the voltages applied to the side electrodes of the coupling region, V_{U} and V_{L}, while keeping V_{T} constant. With a potential detuning, $\Delta = V_{\mathrm{U}} - V_{\mathrm{L}} = 0$ V, the quantum rails are aligned in electric potential and the device serves as a 50-50 beam splitter. Setting a voltage configuration where $\Delta < 0$, the potential of the lower quantum rail (L) is decreased with respect to the upper path (U). For $\Delta > 0$, the situation is reversed.

Deducing the transfer probabilities to the receiver QDs from a thousand single-shot experiments per data point, we measure the partitioning of the electron for different values of Δ as shown in Fig. 3a. Here we sweep V_{U} and V_{L} in opposite directions from -1.26 V to -0.96 V while keeping $V_{\mathrm{T}} = -0.75$ V. The data shows a gradual transition of the electron transfer probability from the upper (U) to the lower (L) detector QD while the total transfer efficiency stays at (99.5±0.3) % – here we do not trigger the sending process. To investigate the role of the tunnel barrier, we perform this measurement for different values of V_{T}. Figure 3b shows the width of the probability transition, σ, as function of the tunnel-barrier voltage. Increasing the tunnel-barrier potential, we find a significant narrowing of the probability transition.

To obtain a better understanding of our experimental observations, we calculate the electrostatic potential along the tunnel-coupled quantum rails[22,23]. We superimpose the dynamic SAW modulation with an amplitude estimated from Coulomb-blockade measurements – for details see Supplementary Section B. Snapshots of the dynamic potential landscape of the tunnel-coupled region are shown in Fig. 3c and Fig. 3d. We investigate the partitioning process of the electron wave function in the double-well potential by employing a very simple stationary model – for details see model A in Supplementary Section C. When we assume pure ground state occupation in the tunnel-coupled region, the model predicts an extremely abrupt probability transition with potential detuning, Δ, that is much narrower than in our experimental observations.

Detaching our model from the assumption of pure ground state occupation, we find a significant broadening of the probability transition with Δ. The prediction of the simple stationary model is in remarkable agreement with the experimental data, if we assume an occupation of excited eigenstates that is exponentially decreasing in energy – see eigenstates in Fig. 3c. In this situation the eigenstate model provides a probability transition (lines in Fig. 3a) that follows the course of a Fermi distribution. Keeping the exponentially decreasing occupation of eigenstates constant, the simple partitioning model predicts, as in our experimental observation, a narrowing of the transition with increased tunnel-barrier potential (line in Fig. 3b). Here the raised tunnel-barrier potential increases the confinement within the potential wells and causes a rearrangement of the eigenstates. This effect is directly reflected in the width of the observed transfer probability transition.

In order to locate the source of electron excitation, we perform time-dependent simulations of the SAW-driven quantum mechanical propagation of the electron along

different parts of our beam-splitter device – for details see model B in Supplementary Section C. As in previous investigations of SAW-driven electron transport[24], we find transitions into excited states at the entrance to the tunnel-coupled region. The change in the potential landscape at this position causes a rapid reconfiguration of the eigenstates in the moving QD leading to Landau-Zener transitions into higher energy states. The time-dependent simulations are in agreement with the stationary model and suggest an excitation energy in the order of a few meV.

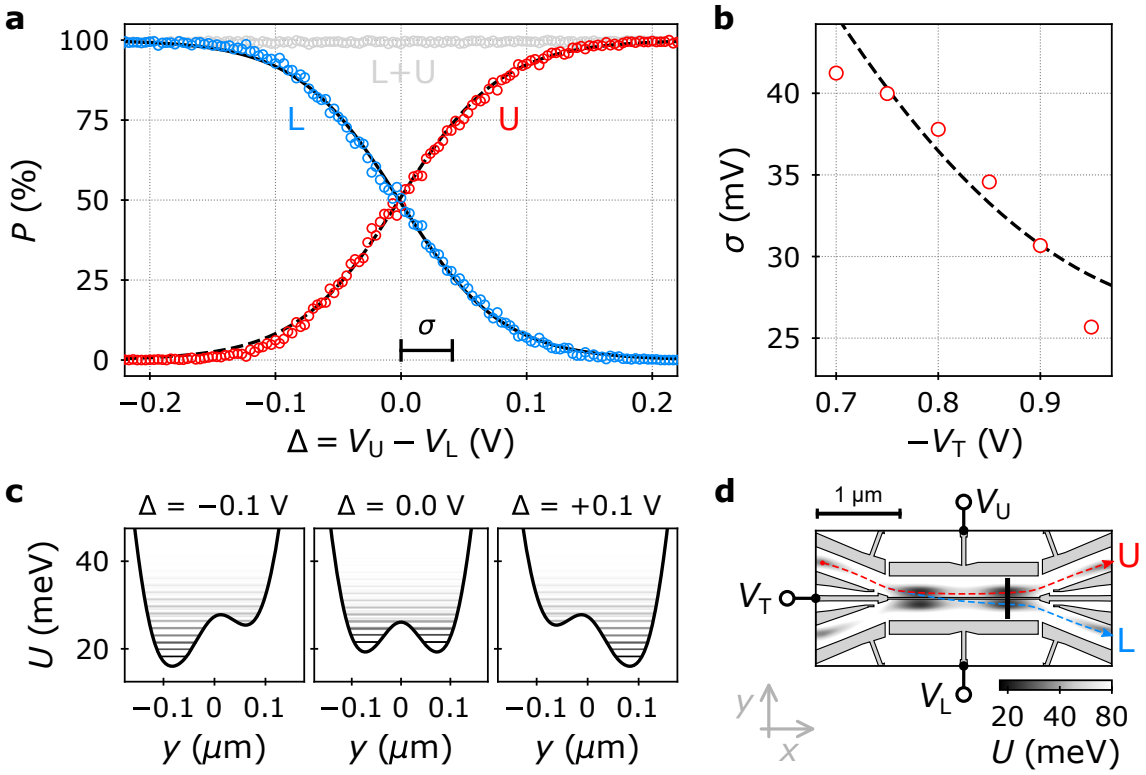

Fig. 3: Partitioning the wave function of an electron in flight. **(a)** Probability, P, for a single electron to end up in the upper (U) or lower (L) quantum rail for different values of potential detuning, Δ. The lines show the simulation result. **(b)** Transition width, σ, for different values of the tunnel-barrier voltage, V_T. The line indicates the stationary model of electron partitioning. **(c)** Slices of the electric potential, U, along the double-well potential. The horizontal lines indicate the eigenstates in the moving QD. The transparency indicates the exponentially decreasing occupation of the states. **(d)** Landscape of the electric potential, U, along the tunnel-coupled quantum rails with SAW modulation. The black spots represent the moving QDs that are formed by the SAW. The vertical bar indicates the position of the aforementioned slice of electric potential.

A flying qubit architecture is an appealing idea to transfer and manipulate quantum information between stationary nodes of computation[4–6]. Thanks to electron confinement during transport and the availability of highly efficient single-electron sources and receivers, SAWs represent a particularly promising candidate to deliver the first quantum logic gate for electronic flying qubits[5,17,18]. Here we have presented two important milestones to tread this path. Using a voltage-pulse trigger, we have demonstrated a powerful tool to synchronise SAW-driven transport of single electrons along parallel quantum rails on a large scale. With this achievement we fulfil an important requirement to couple a pair of single electrons in a beam-splitter setup. Secondly, we have investigated the capability of the present device to partition a single electron from one quantum rail into the other. Employing quantum mechanical simulations, we identified abrupt transitions in the potential landscape as source of charge excitation. We anticipate that an optimised surface-gate geometry as well as stronger SAW confinement[25] and novel material implementations[26,27] will allow coherent propagation of a single electron in a true two-level state[28–31]. Our results pave the way for electron quantum optics experiments[5] and quantum logic gates with flying electron qubits[32] at the single-particle level.

REFERENCES

[1] Hermelin, S. *et al.* Electrons surfing on a sound wave as a platform for quantum optics with flying electrons. *Nature* **477**, 435 (2011).

[2] McNeil, R. P. G. *et al.* On-demand single-electron transfer between distant quantum dots. *Nature* **477**, 439 (2011).

[3] Bertrand, B. *et al.* Fast spin information transfer between distant quantum dots using individual electrons. *Nat. Nanotechnol.* **11**, 672 (2016).

[4] Vandersypen, L. M. K. *et al.* Interfacing spin qubits in quantum dots and donors–hot, dense, and coherent. *npj Quantum Inf.* **3**, 34 (2017).

[5] Bäuerle, C. *et al.* Coherent control of single electrons: a review of current progress. *Rep. Prog. Phys.* **81**, 056503 (2018).

[6] DiVincenzo, D. P. The Physical Implementation of Quantum Computation. *Fortschritte der Physik* **48**, 771–783 (2000).

[7] Flentje, H. *et al.* Coherent long-distance displacement of individual electron spins. *Nat. Commun.* **8**, 501 (2017).

[8] Fujita, T., Baart, T. A., Reichl, C., Wegscheider, W. & Vandersypen, L. M. K. Coherent shuttle of electron-spin states. *npj Quantum Inf.* **3**, 22 (2017).

[9] Mortemousque, P.-A. *et al.* Coherent control of individual electron spins in a two dimensional array of quantum dots. *arXiv:1808.06180* (2018).

[10] Majer, J. *et al.* Coupling superconducting qubits via a cavity bus. *Nature* **449**, 443 (2007).

[11] Roch, N. *et al.* Observation of Measurement-Induced Entanglement and Quantum Trajectories of Remote Superconducting Qubits. *Phys. Rev. Lett.* **112**, 170501 (2014).

[12] Bocquillon, E. *et al.* Coherence and Indistinguishability of Single Electrons Emitted by Independent Sources. *Science* **339**, 1054–1057 (2013).

[13] Dubois, J. *et al.* Minimal-excitation states for electron quantum optics using levitons. *Nature* **502**, 659 (2013).

[14] Ubbelohde, N. *et al.* Partitioning of on-demand electron pairs. *Nat. Nanotechnol.* **10**, 46 (2014).

[15] Barnes, C. H. W., Shilton, J. M. & Robinson, A. M. Quantum computation using electrons trapped by surface acoustic waves. *Phys. Rev. B* **62**, 8410–8419 (2000).

[16] Arvidsson-Shukur, D. R. M., Lepage, H. V., Owen, E. T., Ferrus, T. & Barnes, C. H. W. Protocol for fermionic positive-operator-valued measures. *Phys. Rev. A* **96**, 052305 (2017).

[17] Yamamoto, M. *et al.* Electrical control of a solid-state flying qubit. *Nat. Nanotechnol.* **7**, 247 (2012).

[18] Bautze, T. *et al.* Theoretical, numerical, and experimental study of a flying qubit electronic interferometer. *Phys. Rev. B* **89**, 125432 (2014).

[19] Field, M. *et al.* Measurements of Coulomb blockade with a noninvasive voltage probe. *Phys. Rev. Lett.* **70**, 1311–1314 (1993).

[20] Roussely, G. *et al.* Unveiling the bosonic nature of an ultrashort few-electron pulse. *Nat. Commun.* **9**, 2811 (2018).

[21] Maestri, J. J., Landau, R. H. & Páez, M. J. Two-particle Schrödinger equation animations of wave packet–wave packet scattering. *Am. J. Phys.* **68**, 1113–1119 (2000).

[22] Hou, H. *et al.* Experimental verification of electrostatic boundary conditions in gate-patterned

quantum devices. *J. Phys. D* **51**, 244004 (2018).

[23] Birner, S. *et al.* nextnano: General Purpose 3-D Simulations. *IEEE Trans. Electron Devices* **54**, 2137–2142 (2007).

[24] Kataoka, M. *et al.* Coherent Time Evolution of a Single-Electron Wave Function. *Phys. Rev. Lett.* **102**, 156801 (2009).

[25] Schülein, F. J. R. *et al.* Fourier synthesis of radiofrequency nanomechanical pulses with different shapes. *Nat. Nanotechnol.* **10**, 512 (2015).

[26] Mi, X., Cady, J. V., Zajac, D. M., Deelman, P. W. & Petta, J. R. Strong coupling of a single electron in silicon to a microwave photon. *Science* **355**, 156–158 (2017).

[27] Yoneda, J. *et al.* A quantum-dot spin qubit with coherence limited by charge noise and fidelity higher than 99.9%. *Nat. Nanotechnol.* **13**, 102–106 (2018).

[28] Hayashi, T., Fujisawa, T., Cheong, H. D., Jeong, Y. H. & Hirayama, Y. Coherent Manipulation of Electronic States in a Double Quantum Dot. *Phys. Rev. Lett.* **91**, 226804 (2003).

[29] Petta, J. R., Johnson, A. C., Marcus, C. M., Hanson, M. P. & Gossard, A. C. Manipulation of a Single Charge in a Double Quantum Dot. *Phys. Rev. Lett.* **93**, 186802 (2004).

[30] Petersson, K. D., Petta, J. R., Lu, H. & Gossard, A. C. Quantum Coherence in a One-Electron Semiconductor Charge Qubit. *Phys. Rev. Lett.* **105**, 246804 (2010).

[31] Stockklauser, A. *et al.* Strong Coupling Cavity QED with Gate-Defined Double Quantum Dots Enabled by a High Impedance Resonator. *Phys. Rev. X* **7**, 011030 (2017).

[32] Bertoni, A., Bordone, P., Brunetti, R., Jacoboni, C. & Reggiani, S. Quantum Logic Gates based on Coherent Electron Transport in Quantum Wires. *Phys. Rev. Lett.* **84**, 5912–5915 (2000).

METHODS

Experimental setup

The experiments are performed at a temperature of about 10 mK using a ^{3}He/^{4}He dilution refrigerator. The present device is realised by a Schottky gate technique in a two-dimensional electron gas (2DEG) of a GaAs/AlGaAs heterostructure. The 2DEG is located at the GaAs/AlGaAs interface 100 nm below the surface and has an electron

density of $n \approx 2.7 \times 10^{11}$ cm^{-2} and a mobility of $\mu \approx 10^6$ cm^{2}V^{-1}s^{-1}. It is introduced by a Si-δ-doped layer that is located 55 nm below the surface. All nanostructures are realised by Ti/Au electrodes (Ti: 5 nm; Au: 20 nm) that are written by electron-beam lithography on the surface of the wafer. Applying a set of negative voltages on these surface electrodes, we deplete the underlying 2DEG and form the potential landscape defining our beam-splitter device. Along the quantum rails there are thus no electrons present. The SAW-transported electron is thus completely decoupled from the Fermi sea.

As a SAW source we employ an interdigital transducer (IDT) that is placed outside of the mesa – about 1.6 mm beside our beam splitter. It contains 120 interdigitated double fingers with a finger spacing and width of 125 nm. The wavelength of the generated SAW is thus 1 μm. The aperture of the IDT fingers is 50 μm. We operate the device with a pulse-modulated, sinusoidal voltage signal oscillating at the IDT's resonance frequency of 2.77 GHz. In all of the present experiments the duration of each oscillation pulse on the IDT was set to 30 ns. The power on the signal generator was set to 25 dBm. The signal for the IDT is attenuated by 8 dB attenuators along the transmission line and by 3 dB along the bonding wire. The propagation of evanescent electromagnetic waves from the IDT is suppressed by grounded metal shields. The jitter of the voltage pulse that we send from an arbitrary-waveform-generator (AWG) to the plunger gate of the source QD was deduced as about 6.6 ps (FWHM) with respect to a fixed phase of the SAW burst.

Time-dependent simulations

Knowing the sample geometry, the electron density in the 2DEG and the set of applied voltages, we calculate the electrostatic potential of the gate-patterned device using the commercial Poisson solver NextNano[23] using a frozen charge layer and deep boundary conditions[22]. We deduce a donor concentration of about $1.6 \cdot 10^{10}$ cm^{-2} in the doping layer and a surface charge concentration of about $1.3 \cdot 10^{10}$ cm^{-2}. Superposing the dynamic SAW modulation on the electrostatic potential, we find the eigenstate decomposition of a single electron trapped in a specific moving SAW minimum at a given time. Using the finite-difference method we simulate the two-dimensional evolution of the electron state in this dynamic potential[3]. See Supplementary Section C for more details on the time-dependent solver and the simulations performed.

ACKNOWLEDGMENTS

We would like to acknowledge fruitful discussions with Michihisa Yamamoto. We also acknowledge expert help from Tobias Bautze in the early stage of this project. S. T. acknowledges financial support from the European Union's Horizon 2020 research and innovation program under the Marie Skłodowska-Curie grant agreement No. 654603 and JSPS KAKENHI Grant Number JP18K14082. A. L. and A. D. W. acknowledge gratefully support of DFG-TRR160, BMBF - Q.Link.X 16KIS0867, LU 2051/1-1 and the DFH/UFA CDFA-05-06. X.W. is funded by the U.S. Office of Naval Research. C.B. and P.S. acknowledge financial support from the French National Agency (ANR) and Deutsche Forschungs Gesellschaft (DFG) in the frame of its program SingleEIX Project No. ANR-15-CE24-0035. This project has received funding from European Unions Horizon 2020 research and innovation program under the Marie Skłodowska-Curie grant agreement No. 642688.

AUTHOR CONTRIBUTION

S.T. and H.E. performed the experiment and analysed the data with help from P.-A.M., J.W., G.G., P.S., M.U., T.M. and C.B.. S.T fabricated the sample. H.V.L. developed the theoretical model on time-dependent single-electron SAW propagation under supervision of C.H.W.B and C.J.B.F.. H.V.L., H.E. and X.W. developed the stationary model. A.L. and A.D.W. designed and provided the high mobility heterostructure. All authors discussed the experimental results. H.E., S.T. and H.V.L. wrote the paper with inputs from all authors. C.B. supervised the experimental work.

Supplementary information accompanies this paper.

Competing financial interests: The authors declare no competing financial interests.

Supplementary Information

I. SAW-DRIVEN SINGLE-ELECTRON TRANSPORT

Preparations. In each single-shot-transfer experiment, we perform three steps before launching the SAW train: initialisation, loading and preparation to send. These steps are executed by fast voltage changes on the quantum dot (QD) gates R and C as indicated in the SEM image shown in Supplementary Fig. 4a. In between each step we go to a protected measurement configuration (M) and read out the current through the quantum point contact (QPC) as indicated in the charge stability diagram shown in Supplementary Fig. 4b. Comparing the QPC current before and after each step, we can deduce if an electron entered or left the QD.

To initialise the system, we remove possibly present electrons from all QDs by visiting configuration I. We then load a single electron at the source QD by going to configuration L. Supplementary Fig. 4c shows jumps in QPC current at different loading

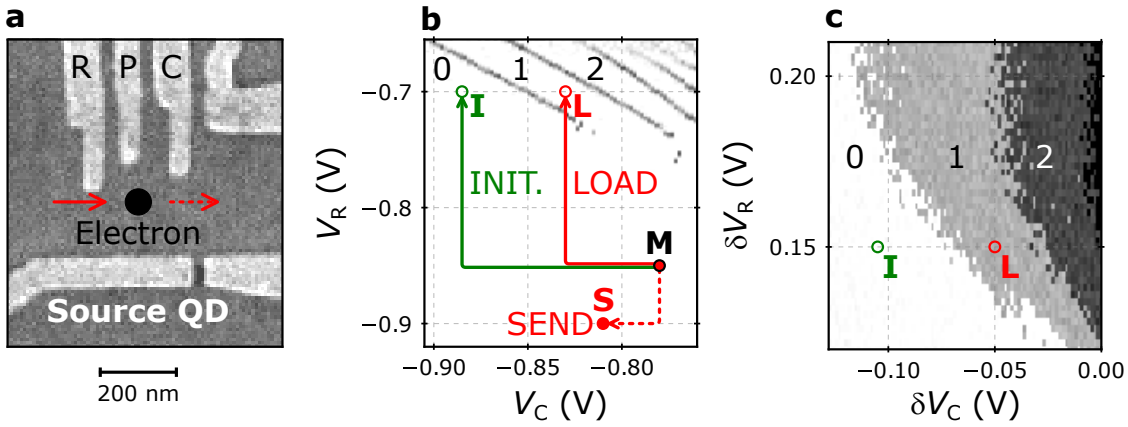

Fig. 4: Preparation of SAW-driven single-electron transfer. **(a)** SEM image of a source QD with indication of surface electrodes. **(b)** Charge-stability diagram showing example source-quantum-dot configurations for QPC measurement (M), initialisation (I), single-electron loading (L) and sending (S). Here we plot $\partial I_{\mathrm{QPC}}/\partial V_{\mathrm{R}}$. The data show abrupt jumps in QPC current indicating charge-degeneracy lines of the QD. **(c)** Loading map showing configurations I and L. Each pixel represents the difference in QPC current, ΔI_{QPC}, before and after visiting the respective loading configuration. The colourscale reflects the electron number in the QD.

configurations (L) that are visited after initialisation via voltage variations from the measurement position, M. The data show that, depending on the voltage variations of the reservoir (δV_{R}) and coupling gate (δV_{C}), different numbers of electrons can be efficiently loaded into the source QD. Having accomplished the loading process, we go to a sending configuration (S) where the electron can be picked up by the SAW. At the same time as we prepare the source QD for sending, we bring the receiver QD into a configuration allowing the electron to be caught. We then launch a SAW train to execute the transfer of the loaded electron. Comparing the QPC currents before and after the SAW burst, we can assess whether the electron was successfully transported.

Sending. In order to find a source QD configuration where the SAW can efficiently pick up a loaded electron, we investigate so-called sending maps. In these maps we compare the QPC currents after and before launching a SAW train. Typical examples are shown in Supplementary Fig. 5. The jump in QPC current, ΔI_{QPC}, is measured both at the source and receiver QDs for various sending configurations that are visited via voltage variation on the reservoir gate, δV_{R}, and the coupling gate, δV_{C}, of the source QD. Here the greyscale is chosen such that a black pixel indicates the presence of an electron.

Supplementary Fig. 5a shows a sending map measured at the source QD where no SAW is sent along the single-electron circuit. The plot shows that the loaded electron can be simply removed from the source QD by the voltage variations, δV_{R} and δV_{C}. The sending map basically shows two transitions: At the horizontal transition (see dashed arrow) the loaded electron is pushed back into the electron reservoir. Trespassing the vertical transition (see solid arrow) on the other hand, the electron is pushed into the quantum rail. Tracing the QPC current at the receiver QD as shown in Supplementary Fig. 5b, we observe no electrons entering, since there is so far no SAW involved.

These transitions shift as we launch a 60 ns long SAW train after bringing the electron at the source QD in the sending configuration – see Supplementary Fig. 5c. This change in the sending map occurs because the SAW allows the electron to overcome the respective potential barriers easier. Investigating ΔI_{QPC} at the receiver QD – see Supplementary Fig. 5d –, we observe an electron entering whenever it was successfully transported by the SAW. The sending position, S, is now chosen such that the electron is only sent to the receiver when a SAW burst is applied. The sending threshold sensitively depends on the SAW amplitude and the potential gradient between the QD and the transport channel[1].

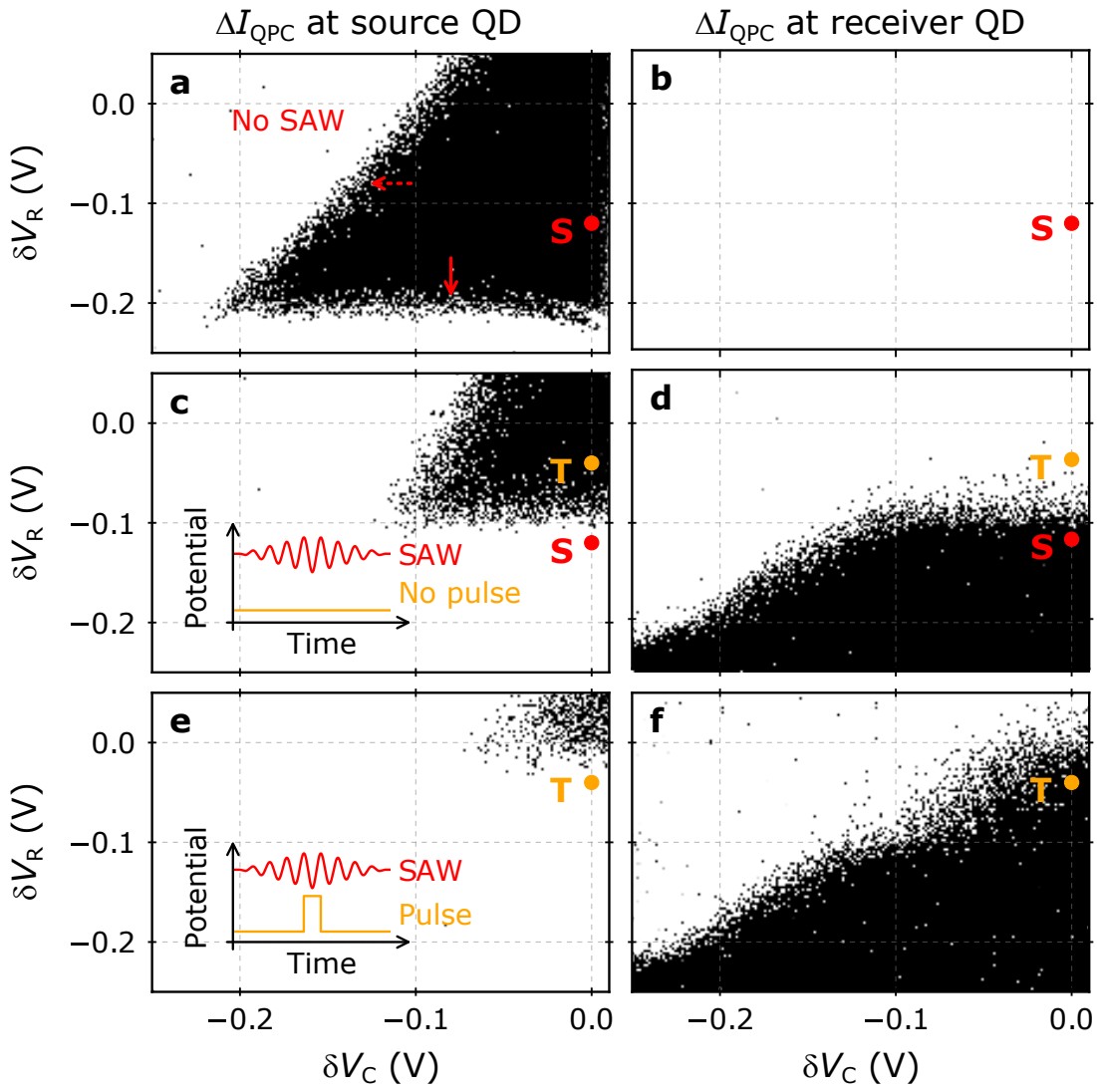

Fig. 5: Exemplary set of sending maps. The plots show jumps in QPC current, ΔI_{QPC}, after a sending configuration is visited via the voltage variations δV_{R} and δV_{C} on the source quantum dot (QD). The colourscale of the plots is chosen such that the black data points indicate events where an electron is present after visiting this position. The voltage configurations S and T indicate possible sending positions without (S) and with (T) additional voltage pulse applied on the plunger gate. **(a)** ΔI_{QPC} measured at source QD without any SAW launched during the sending time frame. **(b)** ΔI_{QPC} measured at receiver QD without SAW. **(c)** ΔI_{QPC} measured at source QD with a 60 ns SAW train launched during the sending time frame. **(d)** ΔI_{QPC} measured at receiver QD showing electron transport by SAW. **(e)** ΔI_{QPC} measured at source QD with additional 360 ps voltage pulse applied at the plunger gate in time with the SAW arrival. (f) Corresponding measurements of ΔI_{QPC} at the receiver QD.

Sending with trigger. To send the electron in a specific moving QD of the SAW train we use a picosecond voltage pulse applied on the plunger gate of the source QD. Supplementary Fig. 5e and Supplementary Fig. 5f show measurements of ΔI_{QPC} at the source and receiver QD for the case where a 360 ps long voltage pulse is applied on the plunger gate (P) of the source QD in time with the arrival window of the SAW. For this pulse a clear shift of the sending transition is apparent. Applying the voltage pulse, the potential barriers are further reduced. Consequently, we can choose a sending position, T, where sending is triggered only by the voltage pulse. Reducing the pulse length down to 90 ps we make the sending fringes visible, but also shrink the region of possible pulse-triggered sending positions, T. As consequence, we find that the most critical factors for the efficiency of this synchronisation approach are the abruptness of the sending transition and the attenuation of the fast pulse along the transmission line.

Efficiency of single-electron transfer. In order to optimise single-electron transfer, we characterise the errors of SAW-driven single-electron transport and specifically treat the limiting factors. In this characterisation procedure we repeat each transfer experiment twice – without and with loading at the source QD after initialisation. Doing so, we can also observe events where the electron is stuck along the transport channel, since in this case subsequent catching events occur when initially no electron was loaded. Supplementary Fig. 6 shows the difference in QPC current, ΔI_{QPC}, before and after SAW transmission at the source (blue) and receiver (green) for thousand single-electron transfer experiments. The grey data shows reference experiments without initial loading at the source QD. The data nicely reflects the extremely high sending efficiency.

Whenever an electron is loaded at the source QD, it is picked up by the SAW causing a positive jump in QPC current – see blue data points in Supplementary Fig. 6a. Thanks to a sufficiently smooth potential landscape along the quantum rail and an optimized catching configuration, the transferred electron also arrives at the receiver QD what causes negative jump in QPC current – see green data points in Supplementary Fig. 6a. In the exemplary data only three catching errors occur. The distinct peaks in the histograms of the events with (coloured) and without (grey) initial loading at the source QD – see Supplementary Fig. 6c-d – show that the presence of an electron in the QD is clearly distinguishable.

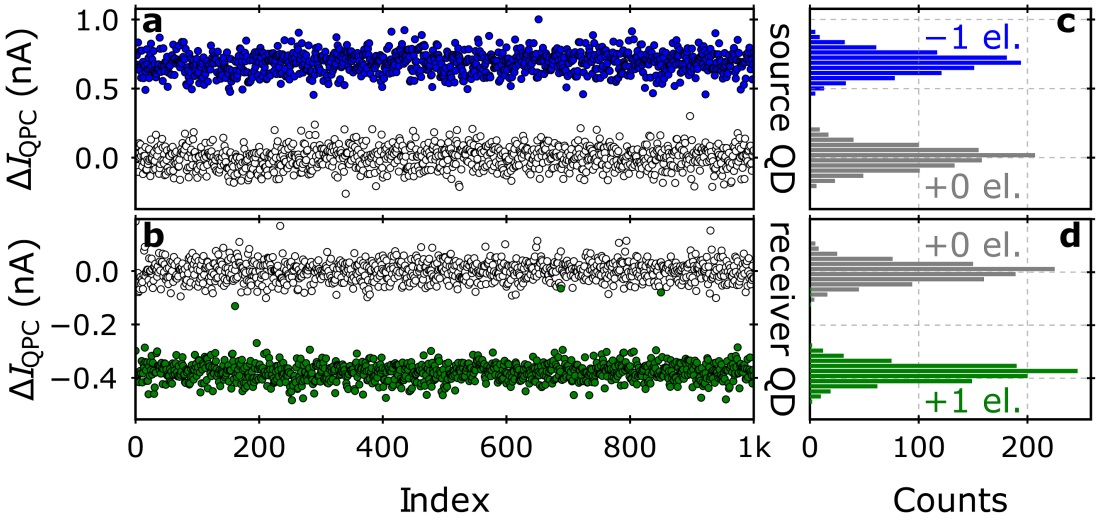

Fig. 6: Characterisation of optimised SAW-driven single electron transport. The data points show the difference of QPC current, I_{QPC}, before and after lauching a SAW train at the **(a)** source and **(b)** receiver QD without (grey) and with (coloured) an electron initially loaded at the source. **(c,d)** Histograms of the data.

II. SAW-AMPLITUDE ESTIMATION FROM COULOMB-BLOCKADE PEAKS

Besides their application as single-electron sources, quantum dots (QDs) can be moreover employed as very sensitive electrometers. Consequently, a QD can be used to measure the amplitude of potential modulation that is introduced by a SAW in piezoelectric materials[2]. The measurement approach is based on the broadening of discrete energy levels in quantum dots by SAW modulation. Due to the piezoelectric coupling, a SAW passing through a quantum dot leads to a periodic modification of the quantum dots chemical potential. This causes that the discrete energy states of the quantum dot oscillate with respect to the bias window. During this process – as for the situation of a classical swing – the quantum dot states remain most of the time close to turning points of the oscillation. Repeating Coulomb-blockade-peak measurements with increased SAW amplitude, the conductance peaks split according to the amplitude of the periodic potential modulation. The two lobes in which such a Coulomb blockade peak splits indicate the two energies at which a quantum dot state stays on average most of the modulation time. Stressing again the classical picture of a swing, thus, one can estimate the peak-to-peak amplitude of the SAW-introduced potential modulation by determining the energy difference between those two lobes of the split peak.

In order to obtain this peak-to-peak amplitude in meV, however, the voltage-to-energy conversion factor η has to be known. This quantity can be determined from Coulomb diamond measurements as exemplary shown in Supplementary Fig. 7a. Knowing η, one can measure the broadening of the Coulomb blockade peaks with rising amplitude of the SAW introduced potential modulation, A. Supplementary Fig. 7b shows an exemplary data set showing the broadening of Coulomb blockade peaks with increasing transducer power, P. The splitting of resonances is indicated by the dashed red lines. At $P \approx 1$ dBm the side peaks of two neighbouring Coulomb blockade peaks start to overlap. At the intersection position, the peak-to-peak amplitude of the SAW is equal to the charging energy of the quantum dot, E_C. The peak-to-peak amplitude of the SAW introduced potential modulation, A, is related to the transducer power, P, by the relation:

$$A\,[\mathrm{eV}] = 2 \cdot \eta \cdot 10^{\frac{P\,[\mathrm{dBm}]-P_0}{20}}, \tag{1}$$

where P_0 is a fit parameter accounting for power losses.

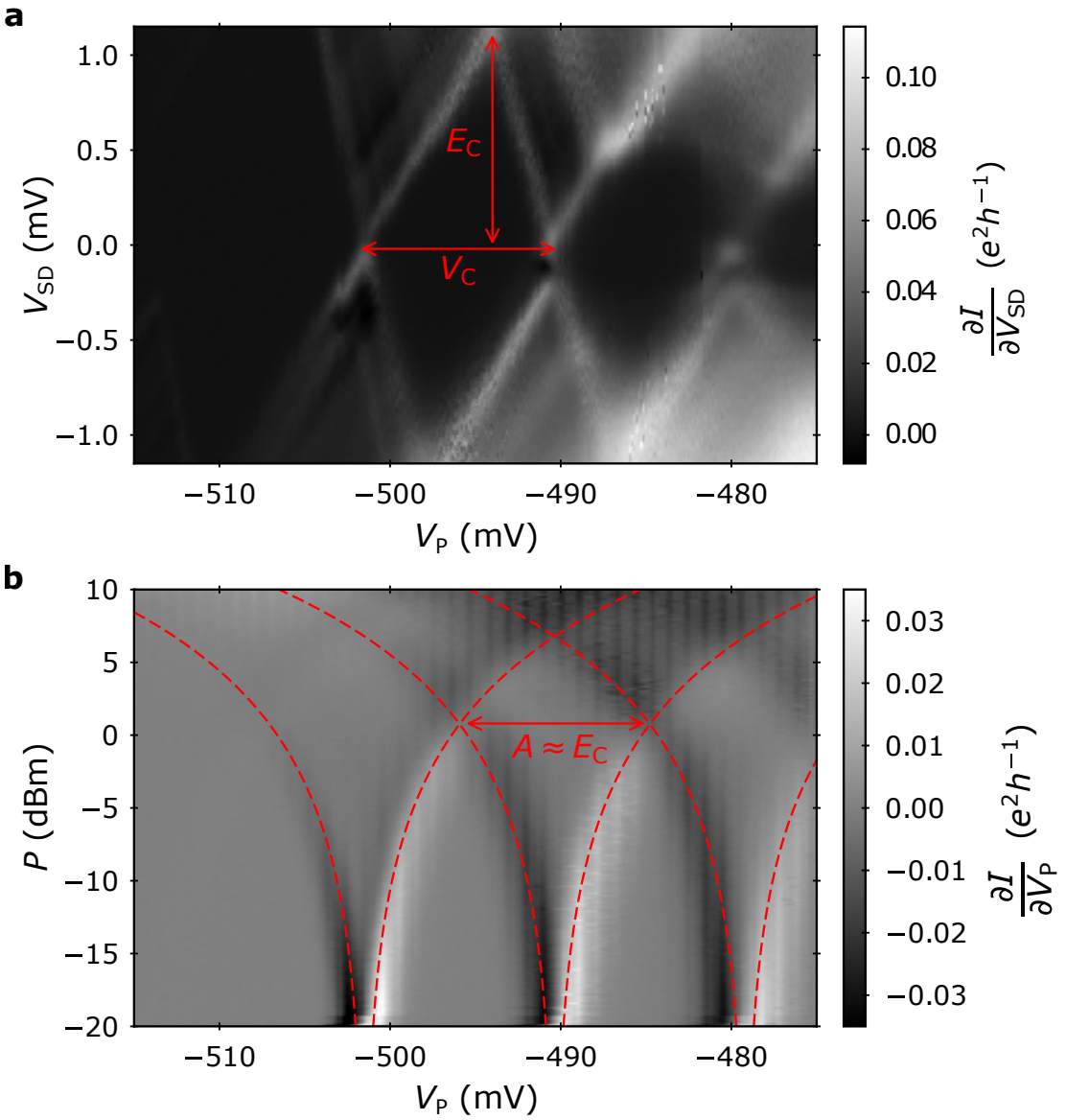

Fig. 7: Exemplary Coulomb diamonds and SAW-introduced peak splitting. **(a)** Measurement of the differential conductance, $\frac{\partial I}{\partial V_{SD}}$, for changes in the source-drain voltage, V_{SD}, and the plunger gate voltage, V_P. The Coulomb diamonds allow deducing the voltage-to-energy conversion factor $\eta = E_C/V_C$. **(b)** Measurement of Coulomb-blockade peaks as the amplitude of a continuous SAW is increased via the transducer power, P. In order to highlight the important features, we plot the derivative of current through the quantum dot, I, with respect to the plunger gate voltage V_P. When neighbouring peaks start to overlap, the amplitude of the SAW introduced piezoelectric potential wave, A, trespasses the charging energy, E_C.

Since these measurements are performed in continuous-wave mode, we trace the broadening of the Coulomb-blockade peaks only up to a transducer power of -5 dBm in order to avoid unnecessary heating. Fitting equation 1 to the data we estimate the SAW amplitude for the typically applied transducer power of 25 dBm with 30 ns pulse modulation. Supplementary Fig. 8 shows the SAW amplitude data (zoom in inset) and the extrapolation to 25 dBm (grey area) for measurements on the present beam-splitter device. The extrapolation indicates a SAW introduced peak-to-peak modulation of about (15 ± 5) meV in the single-electron transfer experiments. Consequently, we modelled the SAW modulation driving single-electron transport in the present beam splitter setup with 15 meV peak-to-peak amplitude.

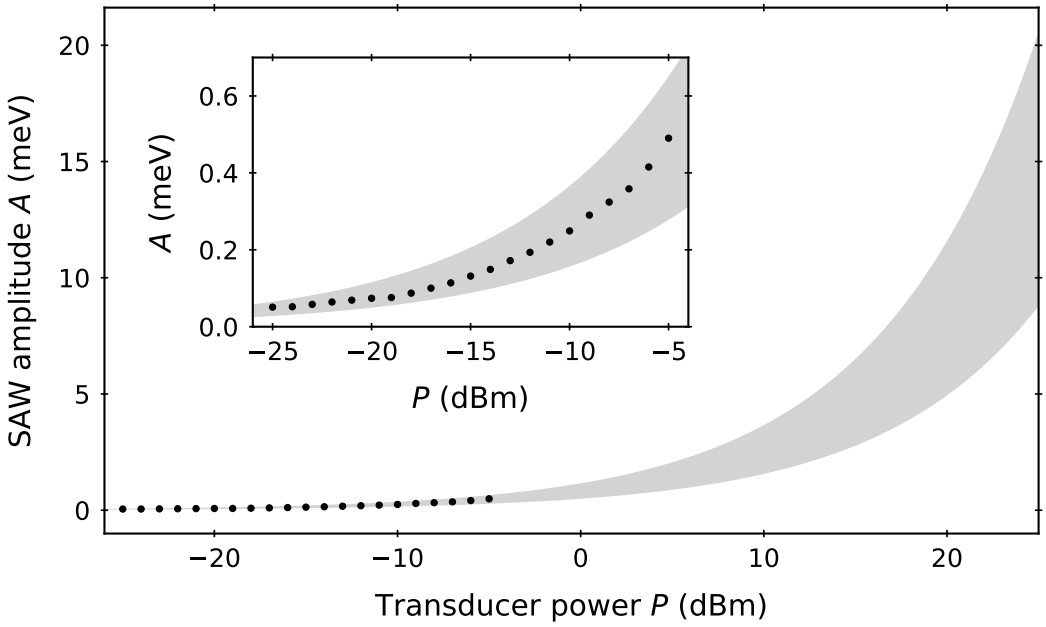

Fig. 8: Amplitude of SAW introduced potential modulation. The data points show the width of the Coulomb-blockade peaks as the transducer power is increased. Comparing the data to equation 1, we estimate the peak-to-peak amplitude with an error that is indicated by the grey area. The plot shows an extrapolation of this region to the typically employed transducer power of 25 dBm. The inset shows a zoom into the data points.

III. QUANTUM MECHANICAL SIMULATIONS

To understand the experimentally observed transition in the transfer probabilities, P_{U} and P_{L}, as function of potential detuning, $\Delta = V_{\mathrm{U}} - V_{\mathrm{L}}$, we employ two independent models. First (model A), we perform a stationary investigation of the eigenstates in the tunnel-coupled region. Secondly (model B), we simulate the time-dependent propagation of the electron within a certain SAW minimum through our device. Model A is a minimum model to understand our data. Model B is more elaborate and accounts for the actual partitioning mechanism. Both give consistent results in agreement with the experimental data.

Model A. Let us begin with the stationary investigation. We consider a one-dimensional cut of the double-well potential in the tunnel-coupling region. In this region we have a sufficiently flat potential landscape, $U(\mathbf{r}) \approx U(y|V) + U_{\mathrm{SAW}}(x,t)$, such that the eigenstate problem becomes separable in the x and y coordinates. The electronic wave function $\phi_i(y)$ along the transverse y direction satisfies the 1D Schrödinger equation:

$$\frac{\hbar^2}{2m_e}\frac{\partial^2\phi_i(y)}{\partial y^2} + U(y|V)\cdot\phi_i(y) = E_i\phi_i(y) \tag{2}$$

where $U(y,V)$ is the electrostatic double-well potential defined by the surface-gate voltages V containing V_{U}, V_{L} and V_{T}. $U(y,V)$ has been obtained from solving the corresponding Poisson problem. m_e indicates the effective electron mass in a GaAs crystal.

To obtain the probability of finding the electron in the upper or lower potential well, we can now simply sum up the contributions from the wave functions of the eigenstates for the respective regions of interest. To obtain the probability of finding the electron in the upper quantum rail, we integrate the square of the wave function over the spatial region of the upper quantum rail:

$$P_{\mathrm{U}} = \sum_i p_i \int\limits_{y>0\ \mathrm{nm}} \left|\phi_i(y, U(y|V))\right|^2 \mathrm{d}y \tag{3}$$

where p_i is the occupation of the eigenstate ϕ_i. For a fixed tunnel-barrier height we can now detune the double-well potential as in experiment by varying Δ. It is now straightforward to calculate the directional coupler transition, $P_{\mathrm{U}}(\Delta, V)$, for the experimental setting with any imaginable occupation of the eigenstates.

Ground state occupation. Let us first consider the situation where only the ground state is occupied. We evaluate equation 3 with mere ground state occupation ($p_0 = 1$) and fixed tunnel-barrier height ($V_\mathrm{T} = -0.7$ V) for different values of potential detuning, Δ, that are changed as in experiment. The predicted course of the probability transition follows the shape of a Fermi distribution:

$$P_\mathrm{U}(\Delta) \approx \frac{1}{\exp(-\Delta/\sigma) + 1} \tag{4}$$

Qualitatively, this course strongly resembles the experimental data. Assuming pure ground-state occupation, the simulation shows that we have to expect an extremely abrupt transition in transfer probability. We can characterise the width of the probability transition by the scale parameter, σ. For pure ground state occupation, the width of the probability transition, σ, is in the order of microvolts. Increasing the tunnel barrier, we increase the confinement in the double-well potential what makes the transition continuously narrower as shown in Supplementary Fig. 9b. For $V_\mathrm{T} \approx -0.9$ V the transition width reaches already a scale of picovolt. With state-of-the art equipment this transition thus would be hardly resolvable in experiment. It would appear as an abrupt jump of transfer probability from 100 % to 0 %.

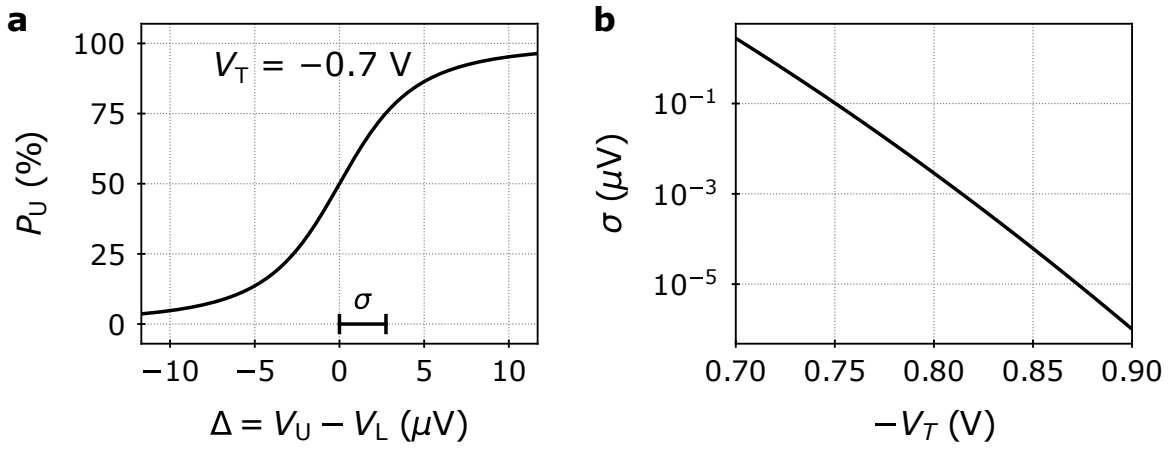

Fig. 9: Partitioning a ground-state electron in the present double-well potential. **(a)** Probability, P_U, to find the electron in the upper quantum rail ($y > 0$ nm) as function of potential detuning, $\Delta = V_\mathrm{U} - V_\mathrm{L}$, for fixed tunnel-barrier height ($V_\mathrm{T} = -0.7$ V). The transition width σ is obtained via the fit of a sigmoid function, $P(\Delta) = 1/(\exp(-(\Delta - \mu)/\sigma) + 1)$. **(b)** Width of the probability transition, σ, for different tunnel-barrier heights defined via V_T.

The role of excitation. Let us now investigate how the situation changes as we populate successively excited eigenstates of the double-well potential. For this purpose we define the occupation of the eigenstates, ϕ_i, with eigenenergies, E_i, via an exponential distribution:

$$p_i \propto \exp\left(-\frac{E_i - E_0}{\varepsilon}\right) \tag{5}$$

where ε is a parameter determining the occupation of higher energy eigenstates. With this approach we can keep the course of the probability transition that resembles the experimental data as we successively occupy excited states. Increasing ε, we find a broadening of the probability transitions as shown in Supplementary Fig. 10a. For $\varepsilon = 6.9$ meV we obtain simulation results of $P_\mathrm{U}(\Delta)$ showing very good agreement over a wide range of V_T. For small values of ε we find an approximately linear relation to the width of the probability transition, σ, as shown in Supplementary Fig. 10b. The slope of this line changes non-linearly as we change the tunnel-barrier height. This shows that the transition width, σ, reflects the occupation of excited states and thus indirectly the confinement in the double-well potential.

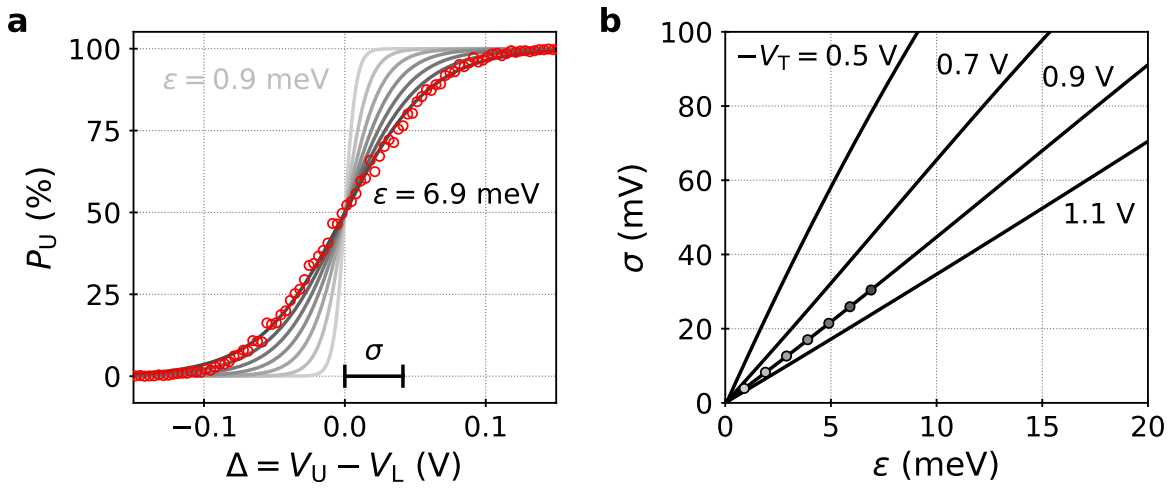

Fig. 10: Partitioning an excited electron in the double-well potential. **(a)** Probability, P_U, to find the electron in the upper quantum rail ($y > 0$ nm) as function of potential detuning, $\Delta = V_\mathrm{U} - V_\mathrm{L}$, for fixed tunnel-barrier height ($V_\mathrm{T} = -0.9$ V). Here we evaluate the stationary model A given by equation 3. The data points show data from experiment. The lines show evaluations of equation 3 for different values of ε. **(b)** Relation between the probability transition width, σ, and the occupation parameter, ϵ, for different tunnel-barrier voltages, V_T.

Model B. Let us now introduce the time-dependent simulation of SAW-driven electron propagation. For this purpose we consider the full two-dimensional potential landscape, $V(\boldsymbol{r},t)$, of our beam-splitter device with a 15 meV peak-to-peak potential modulation of the SAW having a wavelength of 1 μm. We calculate the evolution of the particle described via the electron wave function, $\psi(\boldsymbol{r},t)$, by solving the time-dependent Schrödinger equation:

$$i\hbar\frac{\partial\psi(\boldsymbol{r},t)}{\partial t} = \hat{H}\psi(\boldsymbol{r},t) = \left[-\frac{\hbar^2}{2m_e}\nabla^2 + U(\boldsymbol{r},t)\right]\psi(\boldsymbol{r},t) \tag{6}$$

where $\hat{H}$ describes the Hamilton operator, $U(\boldsymbol{r},t)$ is the two-dimensional dynamic potential encountered by the electron and m_e is the effective electron mass in a GaAs crystal. We numerically solve the equation using the finite-difference method[3] and discretise the wave function both spatially and in time. In one dimension, the single-particle wave function becomes:

$$\psi(x,t) = \psi(m\cdot\Delta x, n\cdot\Delta t) \equiv \psi_m^n \tag{7}$$

where m and n are integers and Δx and Δt are the lattice spacing in space and in time respectively. Following the numerical integration method presented by Askar and Cakmak[4], we evaluate the leading term in the difference between staggered time steps:

$$\psi_m^{n+1} = e^{-i\Delta t\hat{H}/\hbar}\ \psi_m^n \simeq \left(1 - \frac{i\Delta t\hat{H}}{\hbar}\right)\psi_m^n \tag{8}$$

Consequently, we can write the relation between the time steps ψ_m^{n+1}, ψ_m^n and ψ_m^{n-1} as:

$$\psi_m^{n+1} - \psi_m^{n-1} = \left(e^{-i\Delta t\hat{H}/\hbar} - e^{i\Delta t\hat{H}/\hbar}\right)\ \psi_m^n \simeq -2\left(\frac{i\Delta t\hat{H}}{\hbar}\right)\psi_m^n \tag{9}$$

By splitting the wave function in its real and imaginary parts, $\psi_m^n = u_m^n + iv_m^n$, where u and v are real functions, we can evaluate the entire wave function in the same time step. Using the Taylor expansion to estimate the second order spatial derivative, $\frac{\partial^2\psi}{\partial x^2} \simeq \frac{\psi(x-\Delta x)-2\psi(x)+\psi(x+\Delta x)}{\Delta x^2}$, the system of equations to solve becomes:

$$u_m^{n+1} = u_m^{n-1} + 2\left(\frac{\hbar\Delta t}{m\Delta x^2} + \frac{\Delta t}{\hbar}U_m^n\right)v_m^n - \frac{\hbar\Delta t}{m\Delta x^2}\left(v_{m-1}^n + v_{m+1}^n\right) \tag{10a}$$

$$v_m^{n+1} = v_m^{n-1} - 2\left(\frac{\hbar\Delta t}{m\Delta x^2} + \frac{\Delta t}{\hbar}U_m^n\right)u_m^n + \frac{\hbar\Delta t}{m\Delta x^2}\left(u_{m-1}^n + u_{m+1}^n\right) \tag{10b}$$

By this approach we do not need to obtain the eigenstates of the dynamic QD potential for each time step. Instead, we calculate the eigenbasis only at the beginning of the simulation

to form the initial wave function based on an exponentially decreasing occupation of the eigenstates. Solving the system of equations 10 for each successive time step, we then calculate the evolution of the wave function in the dynamic potential landscape that is given by the electrostatic potential defined by the surface gates and the potential modulation of the moving SAW train. We solve the time-dependent Schrödinger equation over the entire tunnel-coupled region using Dirichlet boundary conditions. The boundaries are sufficiently far away from the position of the wave function such that no reflections are observed. To obtain the occupation of the eigenstates after a certain propagation time of the wave packet, we calculate the eigenstates for the potential of the present time step and decompose the wave function in that basis. The method we use is shown to be convergent and accurate.[3]

The origin of excitation. To find the reason for the occupation of eigenstates at higher energies, we simulated the time-dependent SAW-driven propagation of the electron along different sections of our beam-splitter device. Simulating electron propagation along the injection channel, we find no significant excitation in this part of the quantum rail. As we prepare the electron directly after the source QD initially in the ground state, we find that the wave function basically remains in that state after propagation to the entrance of the tunnel-coupling region. We observe only 3 % excitation due to a change in momentum along the angled part of the injection channel.

Simulating the entrance of the flying electron from the injection channel into the tunnel-coupled region, however, we observe an abrupt change in electrostatic potential landscape. Supplementary Fig. 11a shows an exemplary trace (red) of the electron wave function for this situation. The abrupt change in potential confinement causes Landau-Zener transitions into excited states. Supplementary Fig. 11b shows a histogram of the eigenstate occupation after propagation from from the injection channel to the center of the tunnel-coupled region. Comparing this histogram (red) to the exponential distribution (black), we find qualitative agreement of the distributions. Let us note at this point that the employed theoretical models do not take into account relaxation mechanisms. Assuming initial ground state occupation in the injection channel, we obtain an increase of the electrons energy of about 5 meV after propagation to the center of the tunnel-coupled region – see Supplementary Fig. 11c. This value is of the same order of magnitude as the occupation parameter ($\varepsilon = 6.9$ meV) that we use to reproduce our experimental data.

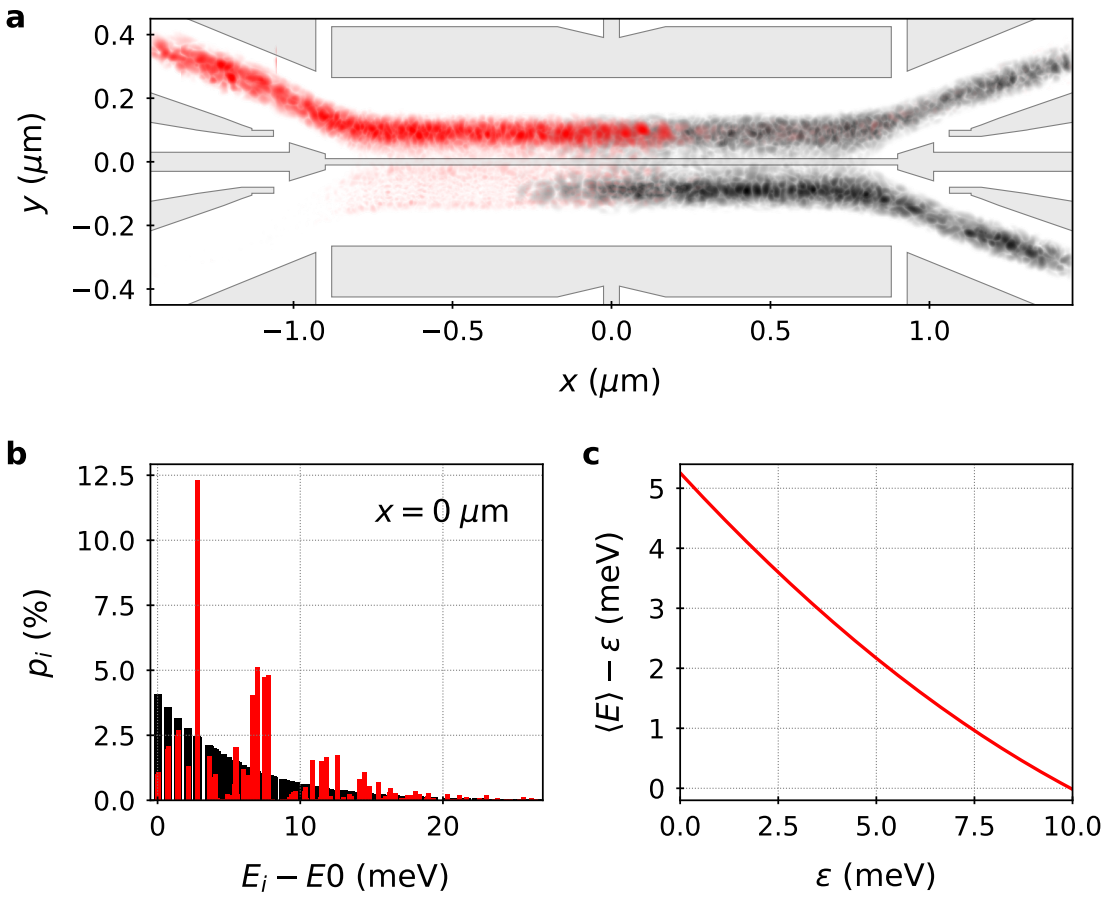

Fig. 11: Comparison of SAW-driven electron transport simulations. **(a)** Propagation of the electron wave function with a moving QD of the SAW along the tunnel coupled region with symmetric potential detuning ($\Delta = 0$ meV) for two scenarios: The red trace shows electron propagation from the injection channel to the center of the tunnel-coupled region. The black trace shows on the other hand electron propagation from the center to the exit of the tunnel-coupled region. For both of the two traces the parameter, ε, determining the initial occupation of excited states was chosen as 6.7 meV. Here the tunnel-barrier voltage is set to $V_T = -0.85$ V. **(b)** Comparison of the eigenstate-occupation distribution, p_i, of the aforeshown red and black traces at the center of the tunnel-coupled region. **(c)** Increase of the expected electron energy, $\langle E \rangle$, due to excitation as function of initial state occupation, ε. Assuming an initial occupation with $\varepsilon \approx 10$ meV, the expectation energy is predicted to remain constant after propagation to $x = 0$ μm.

REFERENCES

[1] Bertrand, B. *et al.* Injection of a single electron from static to moving quantum dots. *Nanotechnology* **27**, 214001 (2016).

[2] Schneble, R. J. *et al.* Quantum-dot thermometry of electron heating by surface acoustic waves. *Appl. Phys. Lett.* **89**, 122104 (2006).

[3] Maestri, J. J., Landau, R. H. & Páez, M. J. Two-particle Schrödinger equation animations of wave packet–wave packet scattering. *Am. J. Phys.* **68**, 1113–1119 (2000).

[4] Askar, A. & Cakmak, A. S. Explicit integration method for the time-dependent Schrödinger equation for collision problems. *J. Chem. Phys.* **68**, 2794–2798 (1978).